

Pure Deep Red Electroluminescence in Mixed Phase **Quasi-2D Tin Iodide Perovskite Heterostructure**

Jesus Sanchez-Diaz, Sergio Galve-Lahoz, Boyu Zhang, Bapi Pradhan, Christian Sternemann, Johan Hofkens, Eva M. Barea, Juan P. Martínez-Pastor, Qing Shen, * Samrat Das Adhikari, * and Iván Mora-Seró*

Mixed cation quasi-2D tin iodide perovskites are promising materials for deep-red to NIR emitting light-emitting diode (LED) applications. However, phase purity remains the major concern to avoid mixed emissions from two or more wavelengths. This work presents the evolution of pure deep red electroluminescence (EL) centred at ≈700 nm corresponding to the emission of pure n = 2 2D crystalline phase. However, structural and optical studies evidenced the formation of mixed-phase heterostructures consisting of n = 1, n=2, and $n=\infty$ phase (i.e., FASnI₃). It is observed that altering the mixed cation ratio, phase distribution is modified, affecting the EL behavior, causing the observation or absence of the n = 1 2D phase EL emission peak. Selective charge transport and their cascade mechanism illustrates the pure color EL evolution with the support from transient absorption spectroscopic studies. In this regard, a case study is provided along with the supportive rationalities behind the exceptional evolution of pure deep red EL even from the mixed-phase perovskite, reported for the first time in case of quasi-2D tin iodide perovskite.

1. Introduction

Metal halide perovskites are receiving considerable attention in the development of the next generation light-emitting diodes (LEDs) due to their exceptional electrical and optical properties.[1-5] Over the last decade, most of perovskite-based LEDs (PeLED) were mainly based on all-inorganic or hybrid organic-inorganic systems, showing outstanding performances^[6-8] but presenting toxic lead (Pb) in their structure. However, tin-based perovskites have emerged as more environmentally friendly and promising candidates to replace leadbased PeLEDs.[9-12] While the 3D lead iodide perovskites are red emitting, 3D tin iodide perovskites emit in the NIR range (e.g., CsSnI₃), and CsSnBr₃ are red emitting $(\approx 677 \text{ nm})$. On the other hand, their 2D Ruddlesden-Popper phase perovskites with single inorganic layer comprised of corner-shared [SnI₆] octahedra structure separated by longer chain organic ammonium cations emit in the visible pure red region ($\lambda_{\rm ex} \approx 630$ nm). [10,12,20] Interestingly, the bandgap of such kind of perovskites is

highly tuneable simply by mixing halides like in lead halide perovskites.[21,22] It is well studied that 2D perovskites bandgap is dependent on the number inorganic octahedra layers separated by the bulky organic cations, conventionally referred as

J. Sanchez-Diaz, S. Galve-Lahoz, E. M. Barea, S. Das Adhikari, I. Mora-Seró Institute of Advanced Materials (INAM) Universitat Jaume I. Av. de Vicent Sos Baynat Castellón de la Plana 12006, Spain E-mail: dasadhik@uji.es; sero@uji.es B. Zhang, Q. Shen

Faculty of Informatics and Engineering The University of Electro-Communications 1-5-1 Chofugaoka, Chofu, Tokyo 182-8585, Japan E-mail: shen@pc.uec.ac.jp

The ORCID identification number(s) for the author(s) of this article can be found under https://doi.org/10.1002/smll.202506221

© 2025 The Author(s). Small published by Wiley-VCH GmbH. This is an open access article under the terms of the Creative Commons Attribution-NonCommercial-NoDerivs License, which permits use and distribution in any medium, provided the original work is properly cited, the use is non-commercial and no modifications or adaptations are

DOI: 10.1002/smll.202506221

B. Pradhan, J. Hofkens Laboratory for Photochemistry and Spectroscopy Molecular Imaging and Photonics Department of Chemistry Katholieke Universiteit Leuven Leuven B-3001, Belgium C. Sternemann Fakultät Physik/DELTA Technische Universität Dortmund 44221 Dortmund, Germany J. P. Martínez-Pastor UMDO Instituto de Ciencia de los Materiales Universidad de Valencia Valencia 46980, Spain S. Das Adhikari Institute of Physical Chemistry

Polish Academy of Sciences

Kasprzaka 44/52, Warsaw 01-224, Poland



www.small-journal.com

"n", where the bandgap decreases with the increase of n, and the general structure in quasi-2D, also known as 2D/3D, is expressed as $L_2(A_{n-1}B_nX_{3n+1})$, where L is the large organic ammonium cation, causing the layered 2D structure, and A is the small monovalent cation, matching in a 3D structure. Taking this into account, n is controlled by controlling the stoichiometry between A cations (e.g., Cs⁺, formamidinium (FA⁺)) and L cations (e.g., 4-fluorophenethylammonium (4FPEA⁺)).[23–27]

The spacer cations play a critical role in controlling the spacing between the individual layers by forming van der Waals interactions.[28,29] This interaction promotes the formation of heterostructures among perovskites with different "n"-values, resulting in the formation of multiple quantum well (MQW) structures.[30] It has been proven that the incorporation of MQWs amplifies the performance of LED devices, where the low-bandgap regions produce EL while the larger bandgap regions help to confine the carriers and protect against nonradiative recombination.[30,31] In addition, energy funnelling from the higher energy to the lower energy facilitates higher LED performance.[32] However, obtaining multi-window emission makes challenging the fabrication of colour-pure LEDs.[33] In a typical case, synthesis conditions and the diverse formation energies of different n-valued perovskites yield the formation of multi-n distributions.[34]

In this work, mixed cation quasi-2D perovskites were prepared using lead-free organic-inorganic hybrid tin iodide perovskites by incorporating two cations: FA⁺ and 4FPEA⁺. The incorporation of these two cations resulted in the formation of quasi-2D layered structured perovskites, maintaining the MQW structure. Due to the difficulties in forming a phase-pure perovskite layer (i.e., pure single n) resulting from their diverse formation energy, heterostructures with different n-valued perovskites were formed following our simple film deposition approach. By controlling the ratio between FA+ and 4FPEA+, different MQWs were formed, evidenced from their structural and optical characterizations. The thickness of the perovskite layer was controlled through the spincoating speed, and the dependence on the film thickness with the EL behaviour has been manifested. The distribution of different phases from the surface to the depth has been analysed by grazing incident wide-angle X-ray scattering (GIWAXS) studies. Despite the presence of multi-peak photoluminescence (PL), single peak EL evolution has been reported, which also depends on the thickness and the mixed cation ratio. Such exotic EL evolution has also been predicted from the transient absorption (TA) spectroscopic analysis.

2. Results and Discussion

Mixed-cation 2D tin iodide perovskite thin films were successfully fabricated by mixing two different chain-length organic ammonium cations, namely, 4FPEA^+ and FA^+ . The resulting films exhibited a layered structure denoted as $(4\text{FPEA})_2\text{FA}_{\text{n-1}}\text{Sn}_{\text{n}}\text{I}_{3\text{n}+1}$, where n corresponds to the number of corner-shared [SnI₆] octahedral layers in the perovskite-like stack. In case of n=1, the structure becomes $(4\text{FPEA})_2\text{SnI}_4$, the thinnest possible inorganic layer without FA⁺ content. Accordingly, for n>1, the smaller FA⁺ cation resides within the octahedral cavities formed by the eight corner-shared [SnI₆] octahedral layers, and 4FPEA^+ controls the interlayer spacing of the inorganic layers. Apparently, the sto-

ichiometry can also be expressed as $(4FPEA)_2(FASnI_3)_{n-1}SnI_4$, which implies that the incorporation of FA+ cation makes thinner unit of FASnI_3, which is strongly quantum confined due to its atomic level thicknesses, and forms multiple quantum well (MQW) structure due to their hierarchical structure, where the spacer cation, $4FPEA^+$ acts as barrier. With the increase of the thickness n, the bandgap decreases. It is noteworthy that the ratio of $4FPEA^+$ to FA^+ is essential to control the value of n.

Herein, different thin films were fabricated by precisely controlling the 4FPEA+/FA+ ratio. To study the dependence of materials properties on the film thicknesses, different spin-coating speeds were systematically adjusted within a range of 1000 (thicker film) to 4000 (thinner film) rpm, further details are provided in the experimental section. Throughout our experimental procedures, the quantity of Sn-precursor was kept constant, while the ratio of the cation precursors were stoichiometrically adjusted, see Table S1 (Supporting Information), and these variations are denoted as "4FPEA:FA:Sn = 2:1:2 (M1)", representing the ideal stoichiometric proportion for n = 2, and "4FPEA:FA:Sn = 2:2:3 (M2)", representing the ideal stoichiometry for n = 3. However, the final films did not manifest exclusively as phasepure perovskites, rather they formed compromised mixed phases involving multiple "n" layers as expected. To understand this behaviour and the mechanisms behind it, we deeply characterized the M1 and M2 films at different thicknesses. Figure S1 (Supporting Information) presents the thicknesses achieved through speed-controlled spin-coating for both compositions, revealing that slower rate, 1000 rpm, led to thicker films, while faster rates, 4000 rpm, conducted to thinner films. The thicknesses were estimated from the cross-sectional scanning electron microscopy (CS-SEM) image, provided in Figures S2 and S3 (Supporting Information).

UV-vis absorbance and X-ray diffraction (XRD) studies were performed for the preliminary characterization of the ndistribution in the fabricated thin films. Figure 1a presents the absorption spectra of M1 at different thickness, which show the different absorbance peak contributions from n = 1 (≈ 614 nm), $n = 2 \ (\approx 677 \text{ nm})$, and the higher n, $n = \infty$, ($\approx 850 \text{ nm}$). The optical bandgaps of these individual phases were estimated using Tauc plots (Figure S4a–c and Table S2, Supporting Information), which involve plotting $(\alpha h \nu)^x$ versus photon energy $(h \nu)$, where α is the absorption coefficient, and x depends on the nature of the electronic transition (herein 2, for direct allowed transitions). The linear portion of the Tauc plot is extrapolated to the energy axis to determine the optical bandgap of each phase. There is a hypsochromic shift in n = 1 bandgap observed with the increase of thickness (from 1.91 to 1.86 eV) that arises from enhanced quantum confinement effects, consistent with thickness-dependent trends in 2D/3D perovskites.[35] However, no shifting has been observed in luminescence properties (shown in a later section). The XRD patterns measured with an incident energy of 8.048 keV presented in Figure 1b, demonstrated mixed-phase contributions from n = 1, 2, and ∞ . At this point, it is convenient to assign the XRD patterns to their corresponding phases. First, the (001) and (002) peaks of 3D $n = \infty$ phase were identified at 14.11° and 28.32°, respectively.[36] Then, we extracted the periodic spacing patterns with the value $\approx 5.37^{\circ}$ (little deviation at higher angles), which belongs to the n = 1 phase. [37,38] Next, the remaining peaks were assigned to the n = 2 phase, where the peaks were nearly

16136829, 2025, 38, Downloaded from https://onlinelibrary.wiley.com/doi/10.1002/smll.202506221 by Universitat Jaume I, Wiley Online Library on [07/11/2025]. See the Terms and Conditions (https://online.library.wiley.com/doi/10.1002/smll.202506221 by Universitat Jaume I, Wiley Online Library on [07/11/2025]. See the Terms and Conditions (https://online.library.wiley.com/doi/10.1002/smll.202506221 by Universitat Jaume I, Wiley Online Library on [07/11/2025]. See the Terms and Conditions (https://online.library.wiley.com/doi/10.1002/smll.202506221 by Universitat Jaume I, Wiley Online Library on [07/11/2025].

onlinelibrary.wiley.com/terms-and-conditions) on Wiley Online Library for rules of use; OA articles are governed by the applicable Creative Commons License

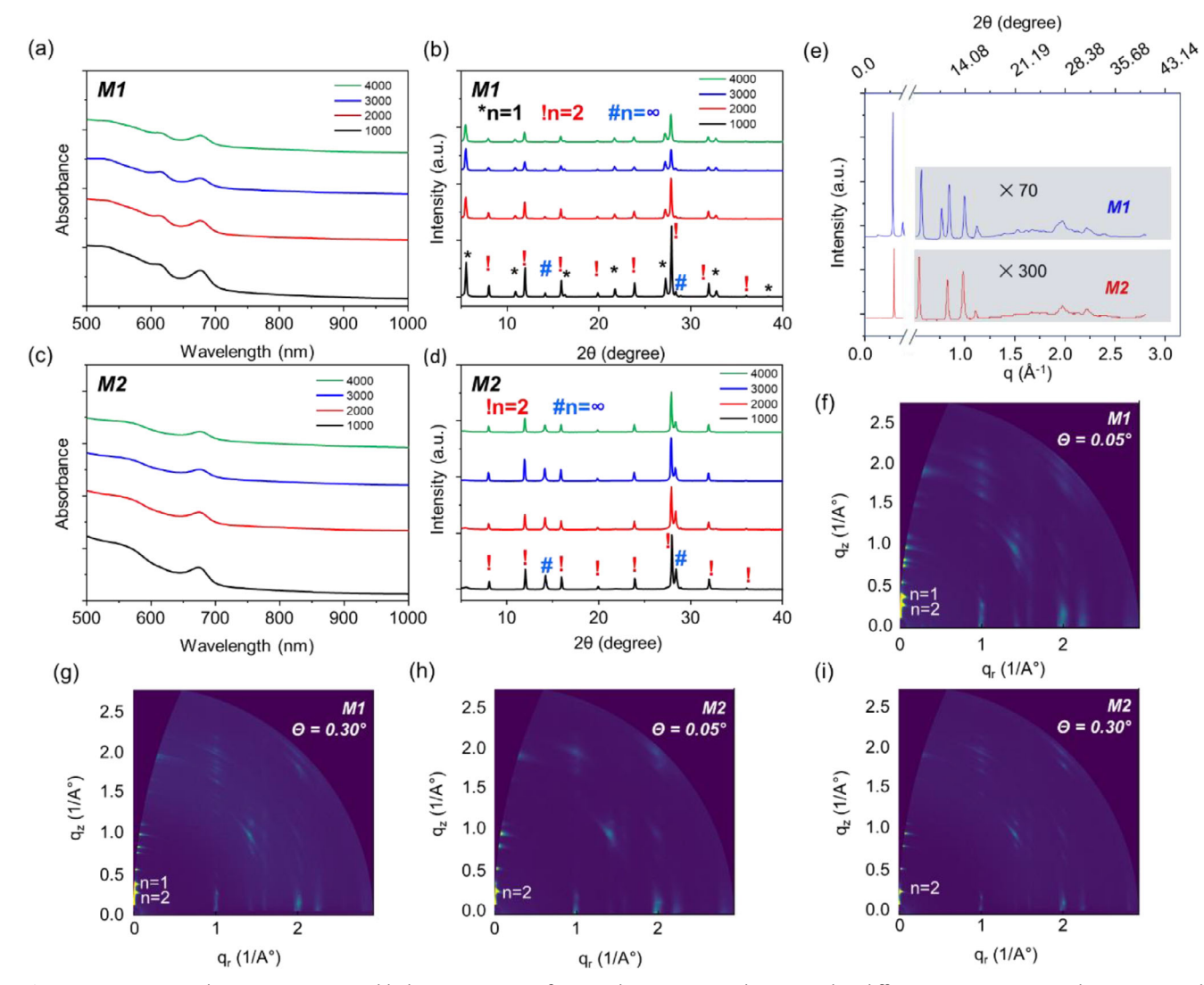


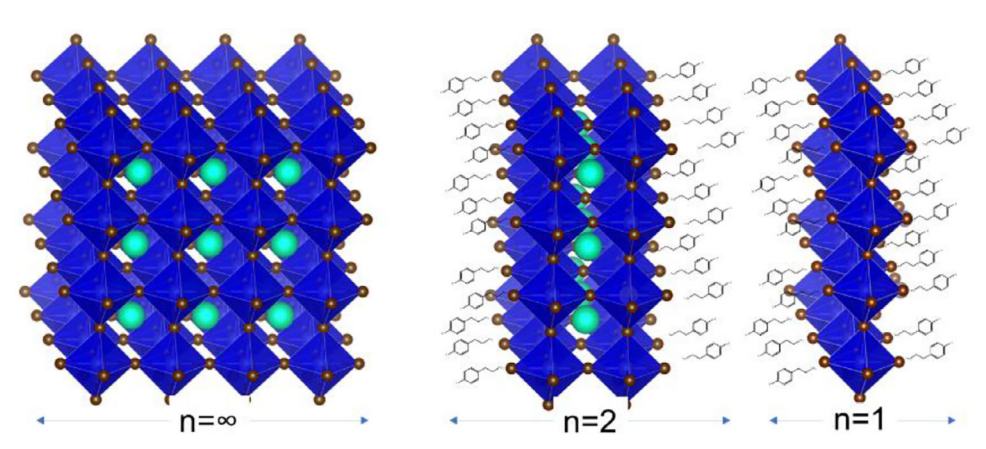
Figure 1. a,c) UV-vis absorption spectra and b,d) XRD patterns of M1, and M2, respectively, prepared at different spin-coating speeds. e) Integrated 2D GIWAXS pattern of M1 and M2 measured at 0.30° incident angle. 2D GIWAXS patterns showing Bragg spots for M1 at f) 0.05° and g) 0.30°, and for M2 at h) 0.05° and i) 0.30°.

periodic as well, with the value \approx 4°. Noteworthy, phases with 2 \leq n \leq ∞ were not observed from the optical characterizations; therefore, XRD patterns with such phases were not assigned. It is important to note that Bragg reflections of $n = \infty$ (i.e., FASnI₃) only belong to the [00*l*] direction, which supports the oriented growth of FASnI₃ along the direction of n = 1 and n = 2 phases. Therefore, arguably it can be confirmed that the different phases is in identical direction and hence forming an MQW structure through heterostructure formation. The XRD peak assignments were further corroborated by UV–vis absorbance, PL, GIWAXS, and transient absorption (TA) spectra, as discussed in the following sections.

Subsequently, perovskite thin films with a higher content of FA⁺, sample M2, were prepared at different spin-coating rates. The UV–vis absorbance spectra are presented in Figure 1c, and the XRD patterns are shown in Figure 1d. The bandgap values of the individual phases are presented in Table S3 (Supporting In-

formation), estimated from the Tauc plot, see Figure \$5a,b (Supporting Information). Notably, with the increase of FA⁺ content, n = 1 phase did not form, while they exhibit distribution of n = 2and $n = \infty$ phases. By comparing the XRD patterns of M1 and **M2**, the peaks from n = 2 and $n = \infty$ are located at the identical position, while n = 1 peaks are missing. For a more comprehensive understanding, Scheme 1 provides a schematic model illustrating different n-valued perovskites, where the bandgap energy decreases as the n value increases, resulting in the anticipated MQW structure. In addition, top-view SEM images (see Figures S6 and S7, Supporting Information) and AFM images (see Figure S8, Supporting Information), were employed to study the film morphology and roughness. Overall, for M1 and M2, an increment in the grain size with the increase of thickness (i.e., at lower rpm) is observed. This may be due to the slow crystallization process during the film formation, as a result of the saturation of the solvent in the wet film. Similar case happens with the film





Scheme 1. Schematic model illustrating different n-valued perovskites.

roughness, the thicker the film the more roughness it has, e.g. for M1 the root mean square roughness (R_o) at 4000 rpm was estimated to be 7.12 nm, while for 1000 rpm 22.15 nm (see Table S4, Supporting Information, for other estimated roughness), this increase of roughness can be due to the uncontrolled crystallization when the film is formed, due to the slow solvent evaporation. Surface potential mapping via Kelvin probe force microscopy (KPFM) reveals distinct surface patterns in M1 and M2, which could be attributed to phase distribution driven by different perovskite dimensionality (n-value), see Figure \$9 (Supporting Information). Contact potential difference (CPD) mapping gives important clues of the phase distribution depending on the type of samples (M1 or M2) and the sample thickness. Sample thickness does not introduce a major variation on CPD, just lower surface phase homogeneity is observed when film thickness increases. On the other hand, M2 samples present higher CPD than M1, stressing the change in the surface phase distribution depending on the precursor composition.

GIWAXS measurements were carried out to investigate the mixed phase distribution in the thin films. By altering the incident angle, depth profile analysis was carried out for M1 and M2 for the thicker samples (1000 rpm). The chosen incident angles Θ_i were: 0.05°, 0.08°, 0.15°, and 0.30°, in order to vary the probing depth with $\Theta_i = 0.05^{\circ}$ providing the highest surface sensitivity. In accordance with the XRD patterns, 2D GIWAXS patterns were matched for M1 and M2 samples prepared at 1000 rpm, and contributory peak positions from different phases were assigned, see Figure 1e and Table S5 (Supporting Information) at 0.30° incident angle. The peaks from n = 1 and n = 2 phases showed repetitive patterns of $\approx 0.38 \text{ Å}^{-1}$ and $\approx 0.276 \text{ Å}^{-1}$, respectively. 2D GIWAXS patterns presented in Figure 1f-i show Brags spots. The Bragg reflections show a strong orientational dependence, which confirms the alignment of the films in [00l] direction. We have analysed the n = 1 and n = 2 phase distribution of M1 thin films along the film depth by studying their Bragg peak intensities varying with the incident angle. The ratio of 2D GIWAXS peak intensities at $q = 0.384 \text{ Å}^{-1}$ and $q = 0.283 \text{ Å}^{-1}$ of n = 1 and n = 2 phases, respectively, was calculated and plotted against the incident angle, see Figure \$10 (Supporting Information). At the lower incident angles, higher n = 1 phase proportion was observed compared to the n = 2 phase, while the n = 2 phase remained predominant over the n = 1 phase at the depth. To summarise, M1 sample consists predominantly of n = 1 phase at the surface of the film predominantly, while its population decreases over n = 2 phase in the depth.

Figure 2 presents the steady-state photoluminescence (PL) and PL excitation (PLE) spectra for M1 and M2 at 1000 rpm and 4000 rpm, where the PL emission peaks originate from n = 1, 2, and ∞ appeared at 625, 695, and 880 nm, respectively. The PLE spectra correspond to the n = 1 phase (blue curve), n = 2 phase (green curve), shoulder peak at \approx 775 nm (red curve), and $n = \infty$ phase (yellow curve). Noteworthy, n = 1 phase is not present in M2, and the shoulder peak is only present at 1000 rpm of M1. The shoulder PL peak is observed at 775 nm could potentially originate from a small contribution of the n = 3 phase, see Figure 2a. However, it is evident that this phase does not show any distinct optical absorption in the PLE spectra. Instead, the only resonances exciting this PL contribution at 775 nm are those associated with the ground exciton and the excited state of the n = 2 phase (compare with the green spectrum in the same figure). Notably, the relative PL intensity is higher in the thicker films (1000 rpm) compared to the thinner films (4000 rpm), with a percentage of \approx 279% in case of M1, and \approx 71% in case of M2. A similar trend was also observed for the XRD analysis. In particular, the PL intensity of the $n = \infty$ phase centred at 880 nm, exceeded that of the lower n phases. This difference in intensity can be attributed to the well-known phenomenon of energy funneling, where excitons (bounded electron-hole pairs) with higher energy generated in the lower n (higher bandgap) perovskites transfer to the higher n (lower bandgap) perovskites with a lower bandgap.

The PLE intensity at the exciton resonance of the n=2 phase (in both PLE spectra detected at 880 and 700 nm) decreases in sample M1 at 1000 rpm compared to that in sample M1 at 4000 rpm and in both M2 samples (at 1000 and 4000 rpm). The exciton resonance of n=2 is clearly observed in PLE (highlighted by green shaded regions in Figure 2), as is the exciton corresponding to n=1 (blue spectra, blue shaded regions). The exciton resonance of $n=\infty$ is not typically observed as a distinct peak, similar to what is seen in FASnI $_3$ films. [39,40] Instead, a near-linear increase in emission intensity is observed for excitation wavelengths below 880 nm. This behaviour also evident in the absorption spectra shown in Figure 1, is attributed to the significant inhomogeneity of the film, which results in a broad PL band (>70 nm) and the low optical oscillator strength of 3D

16136829, 2025, 38, Downloaded from https://onlinelibrary.wiley.com/doi/10.1002/smll.202506221 by Universitat Jaume I, Wiley Online Library on [07/11/2025]. See the Terms and Conditions (https://onlinelibrary.wiley.com/terms

and-conditions) on Wiley Online Library for rules of use; OA articles are governed by the applicable Creative Commons License

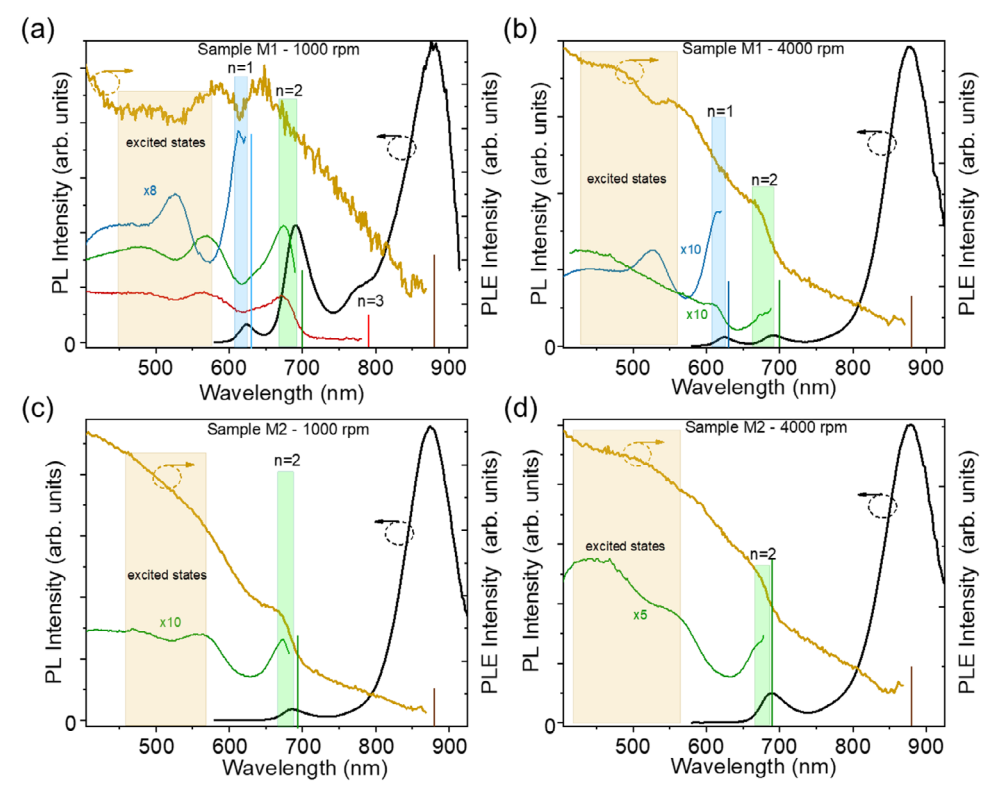


Figure 2. PL and PLE spectra of samples a) M1 at 1000 rpm, b) M1 at 4000 rpm c) M2 at 1000 rpm, and d) M2 at 4000 rpm. PL spectra were recorded at 405 nm excitation. The PLE spectra correspond to the n = 1 phase (blue curve) 625 nm, n = 2 phase (green curve) 695 nm, shoulder peak at \approx 775 nm (red curve), and $n = \infty$ phase (yellow curve) 880 nm.

excitons in FASnI₃ compared to those of 2D (n=1) and near-2D (n=2) exciton transitions. It is evident that the film thickness influences the concentration of photogenerated carriers in PL experiments through the term [1-exp(- α d)], where α is the absorption coefficient (which increases with photon energy for both the $n=\infty$ and also for 2D/near-2D phases due to their stronger exciton oscillator strengths), and d is the film thickness. Accordingly, at a given excitation wavelength (e.g., 405 nm; used in the PL measurements), the photogenerated carrier concentration will be higher in the films prepared at 1000 rpm for both samples, since their thicknesses are approximately double those of the films prepared at 4000 rpm, see Figure S1 (Supporting Information).

To investigate the electroluminescent properties of the perovskite thin films and their phase distribution effects, LED devices were fabricated following the device structure: ITO/PEDOT/Perovskite/PO-T2T/LiF/Al, [42] see Figure S11 (Supporting Information). The obtained electroluminescence (EL) spectra from different stoichiometries at various spin-coating rates are provided in Figure 3. Interestingly, as mentioned above, the EL trend differed significantly between M1 and M2 in terms of the (i) the origin of emission, and (ii) EL intensity versus film thickness. Figure 3a shows EL spectra of M1, where the only single peak from n = 2 phase, located at 700 nm is originates with an average bandwidth of ≈42.8 nm, which is considerably narrower and promising for display applications. It is important to note that, despite the presence of mixed phases, evidenced from the previously discussed optical and structural characterizations, the device only showed the phase-pure EL from the n = 2 phase.

To best of our knowledge, this is the first report of illustrating pure color EL of quasi-2D tin iodide perovskite MQW. Noteworthy, 3D CsSnBr₃ perovskites are also deep red emitting centred at 677 nm.^[19] The thickness of the active layer played an important role to control the EL intensity and thus, the device performance, see Figure S12a,c (Supporting Information), which consistently

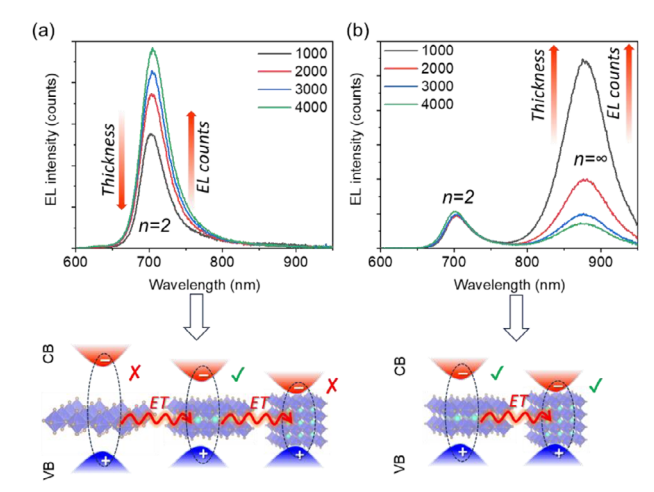


Figure 3. EL spectra of a) M1, and b) M2 at various thicknesses. The bottom panels of each plot represent presenting the possible recombination pathways and the obtained ELs, where ET, VB, and CB stand for energy transfer, valence band, and conduction band, respectively.

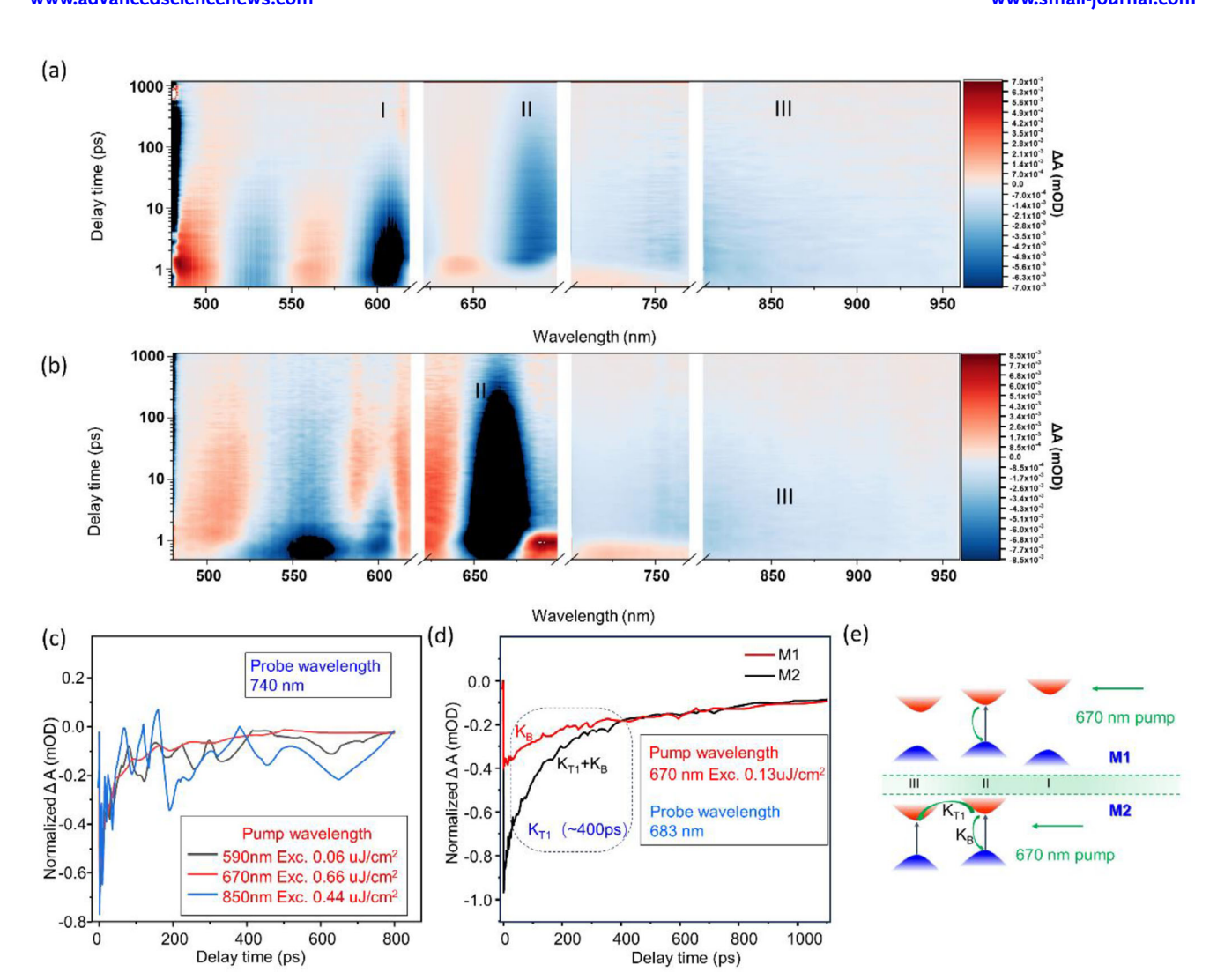


Figure 4. TA mapping of a) M1 and b) M2 at 470 nm excitation wavelength. c) TA bleach dynamics of sample M1 with the pump wavelengths 590 nm (black plot), 670 nm (red plot), and 850 nm (blue plot). d) A comparison to the TA bleach dynamics of Sample M1 and M2 at 670 nm pump wavelength and 683 nm probe wavelength, and e) its corresponding schematic.

decreases with the increase of thickness (i.e., decreasing rpm). With increasing thickness, EL performance typically declines because internally emitted photons are prone to being trapped or reabsorbed due to the overlap between the material's emission and absorption spectra. [43] Additionally, thinner active layers exhibit enhanced radiative recombination due to increased charge carrier density, further improving EL performance. Figure \$13 (Supporting Information) presents an integral EL intensity versus voltage plot, and the luminance-current density plots, respectively, which show higher EL intensity at lower voltages, thereby suggesting that thinner layer devices exhibit earlier EL onset and higher EL output at comparable current densities, suggesting more efficient radiative recombination stemming from higher carrier density. Figure 3b provides EL spectra of M2 at different thicknesses, where the evolution of dual EL peak has been noted, one contribution from n = 2 located at 700 nm (FWHM \approx 44 nm), and the other contribution is from $n = \infty$, located at 880 nm (FWHM \sim 67 nm). While the peak intensity of n=2 has nearly no change in intensity with the increase of thickness, the EL intensity of the peak centred at 880 nm ($n=\infty$) has exactly the opposite trend to the former, descending order of intensities with the increase of spin coating speed (i.e., decrease of thickness). To further investigate this ambiguity, we fabricated pure FASnI₃-based devices, where we observed the ascending order to the EL intensity with the decrease of thickness, exactly opposite to the EL trend observed in M2 (thinner film), shown in Figure S14 (Supporting Information). The EL peak position of NIR emitting FASnI₃ is centred at 881 nm, corroborates well with the $n=\infty$ data of M2.

A clear contrast between EL and PL spectra is observed for M1, where the PL spectra show all the emission contribution from all the phases, see Figure 2a, while the EL originated purely from the n=2 phase, see Figure 3a. It is anticipated that the role of selective charge injection plays a crucial role in this ambiguity. On the other hand, M2 shows dual emission originated from both n=2 and $n=\infty$ phases, similar trend to the PL spectra.

www.small-journal.com

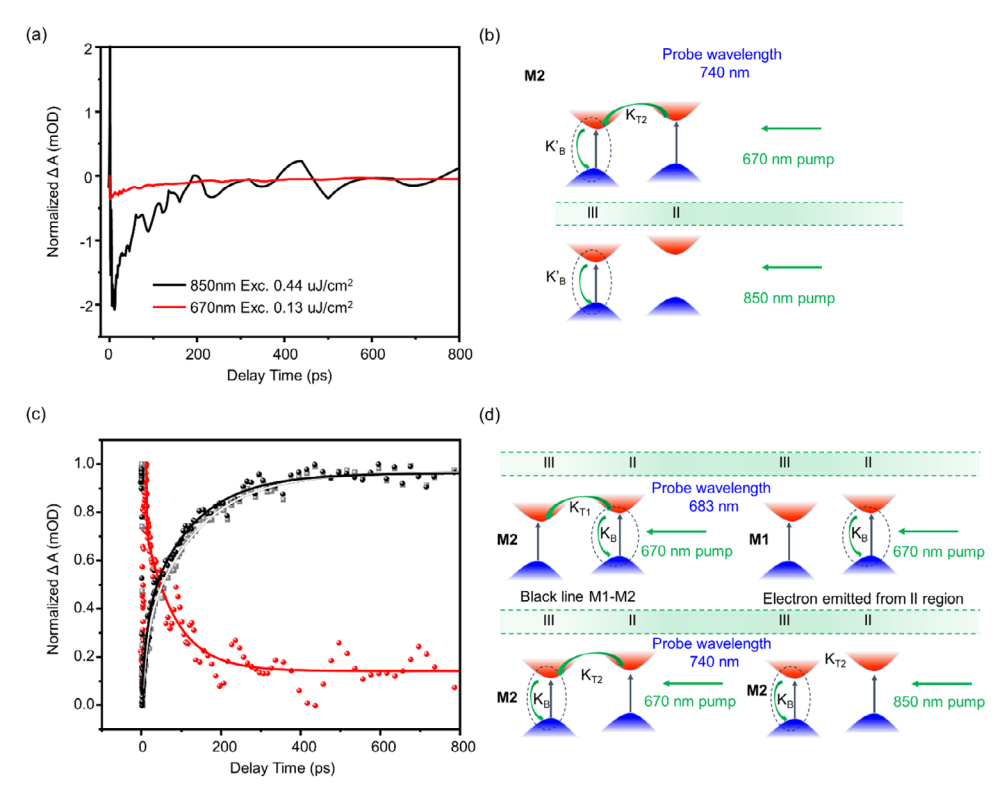


Figure 5. a) Comparison of TA bleach dynamics of M2 by exciting at 670 nm (black plot), and 850 nm (red plot), fixing the probe wavelength at 740 nm, and b) its corresponding schematic. c) The black curve corresponds to the difference in dynamics at the n=2 bleach position between the M1 and M2 samples under 670 nm excitation (The influence of defects has been removed. The grey curve represents the case with defect effects retained.), reflecting the electron transfer process from the n=2 state to the $n=\infty$ state. The red curve corresponds to the difference in dynamics at the $n=\infty$ position for the M2 sample under 670 and 850 nm excitation, representing the process of electron acquisition at the $n=\infty$ state originating from the n=2 state. d) Schematic explanation of Figure (c).

To shed light onto the charge transfer mechanisms of the different prepared samples we performed TA analysis. From this analysis, we have identified three radiative recombination pathways for M1, located at \approx 600, \approx 700, and 830 nm, named as I, II, and III, respectively. These radiative recombination pathways are in line with the peaks observed in the UV-vis absorption and PL spectra showed in Figures 1a and 2a, respectively, and depicted in Figure 3a (bottom panel). On the other hand, only two radiative recombination pathways have been observed for M2, centered at ≈700, and 830 nm for II and III, respectively, which also agrees with the peaks observed in UV-vis absorption and PL spectra presented in Figures 1c and 2c, respectively, and shown in the bottom panel of Figure 3b. The Corresponding TA mapping from which we identify the recombination pathways of M1 and M2 is provided in **Figure 4**a,b. Furthermore, to understand the radiative recombination and electron transfer dynamics in M1, we have excited with the three different pump wavelengths at 590, 670, and 850 nm identified from the TA mapping, see Figure 4a,b, and the probe wavelength was 740 nm to study their bleach dynamics and investigate possible charge transfers from high energy states (i.e., n = 1 and n = 2) to the lower energy state $n = \infty$. Figure 4c shows TA bleach dynamics spectra for sample M1, where no noticeable difference in the bleach dynamics is observed, suggesting that there is no charge-transfer process occurring from n = 1to $n = \infty$, nor from n = 2 to $n = \infty$ in sample M1. This observation explains the absence of EL emission from $n = \infty$ (880 nm)

in the case of M1, which explains the pure color emission from n = 2 in M1. Furthermore, by comparing the TA bleach dynamics of M1 and M2 spectra fixing the pump wavelength at 670 nm and probe wavelength at 683 nm, we can observe the possible charge transfer dynamics from n = 2 to $n = \infty$. As we can observe from Figure 4d, there is a large difference in the charge transfer dynamics between M1 and M2 of ≈400 ps, which suggests the charge transfer from n = 2 to $n = \infty$ in M2, and could explain the dual peak in the EL for M2. Figure 4e presents a schematic illustration of the discussed mechanism. This observation goes in line with GIWAXS studies, see above comment regarding Figure S10 (Supporting Information), which revealed that the top surface of the thin film of M1, has n = 1 rich phase, therefore the electron injection from the electron injection layer (EIL), selectively goes through the n = 1 phase, which further funneled and recombine radiatively at the n = 2 phase. At the same time, the bottom layers consist of n = 2 rich phase, and hence the holes injected from the hole injection layer (HIL) are injected into the n = 2 rich phase, and cannot be further injected into the n = 1 phase due to unfavorable band alignment, avoiding the EL from n = 1 phase in

Furthermore, looking at the XRD pattern of M1 sample, see Figure S15 (Supporting Information), specifically at the diffraction peak at angle 14.1°, that corresponds to the FASnI $_3$ phase ($n=\infty$), arguably it can be stated that the proportion of FASnI $_3$ phase in M1 is low and significantly lower than in M2, as



consequence in M1 injected electron and hole recombine preferentially in the n=2 phase before can be funneled into the low amount 3D $n=\infty$ phase with narrower bandgap. The small amount of 3D $n=\infty$ phase also explains why there is no change in the bleach dynamics of III, independently of the excitation wavelength, as photoexcited charges recombine before they can find a way to be injected, both electrons and holes, into the 3D phase.

A similar analysis has also been carried out for M2 samples, which provides a clearly different behavior than M1. The TA bleach dynamics spectra were studied at different pump wavelengths, 670 and 850 nm, keeping the probe wavelength at 740 nm. As shown in Figure 5a, when the pump wavelength was set to 670 nm, exciting both n = 2 and $n = \infty$, and 850 nm, selectively exciting $n = \infty$, the bleach dynamics at 740 nm exhibited a clear difference within the short-lived regime (≈200 ps). This observation indicates a charge transfer process from n = 2to $n = \infty$ in M2, which is also consistent with the EL spectrum. A schematic of the charge transfer mechanism is presented in Figure 5b. For M2 sample, the amount of $n = \infty$ phase is significantly higher than in M1 and consequently funneling are produced before recombination in n = 2 phase. To investigate the interlayer carrier transfer behaviour in detail, a systematic evaluation was performed, as shown in Figure 5c. In this analysis, the M2 sample was excited at 670 and 850 nm, and the bleach dynamics were monitored at 740 nm (corresponding to the $n = \infty$ state). Under 670 nm excitation, the dynamics at 740 nm include not only the bleach dynamics corresponding to the $n = \infty$ state but also the electron transfer processes from other states to the $n = \infty$ state. Under 850 nm excitation, only the bleach dynamics corresponding to the $n = \infty$ state was observed. The difference between these two curves represents the electron acquisition process at the $n = \infty$ state (the red curve in Figure 5c) from n = 2 state. Additionally, under 670 nm excitation, the bleach dynamics at 683 nm (corresponding to the n = 2 state) were compared between M1 and M2 samples. It was confirmed in previous discussions that the M1 sample did not exhibit transfer to lower energy states, whereas the M2 sample did. The difference between these dynamics reflects the electron transfer from n = 2to lower energy states (the grey curve in Figure 5c). Notably, the grey and red curves are expected to exhibit complementary dynamics if the electron transfer is solely from n = 2 to $n = \infty$. However, the experimental results deviate from this expectation, suggesting the involvement of a competing defect-capture process during the charge transfer. To further explore this, we investigated the bleach dynamics under 670 nm excitation. At a probe wavelength of 683 nm, typical bleach behavior was observed. Interestingly, as shown in Figure S16a (Supporting Information), the dynamics at 709 nm differ significantly from those at 683 nm. This discrepancy implies the presence of trap states near the n = 2phase, consistent with the charge transfer mechanism proposed in Figure S16b (Supporting Information) and further supported by the carrier extraction kinetics in Figure \$16c (Supporting Information). Furthermore, the grey curve was fitted and corrected to eliminate the contribution of the defect-related process. The resulting black curve (Figure 5c) shows complementary behavior with the red curve, thereby confirming the influence of defectmediated capture during the electron transfer process. All these studies suggest that the M2 sample possesses two transfer pathways for n=2, (i) the capture of defect states, and (ii) the transfer to $n=\infty$, as proposed in Figure 5d. The absorptivity of region III and the EL intensity for samples of different thicknesses is verified by plotting EL intensity versus absorptivity, see Figure S17 (Supporting Information), where the nonlinear relation indicates that defects vary with thickness. The proportion of defect state capture in the total transferred electrons in the M2 sample is assumed to be related to the thickness of the film. That is, the thicker the film, the smaller the proportion of defect states and hence more energy transfer to $n=\infty$, resulting in the increase of EL intensity with the thickness, as shown in the EL spectrum from the M2 LEDs.

3. Conclusion

Deep red emission centred at 700 nm has been demonstrated for the first time in tin iodide perovskites. By incorporating the longchained spacer cation 4FPEA+ into 3D tin iodide perovskites, the bandgap was effectively tuned to produce pure color deep red EL with a narrow full-width at half-maximum (FWHM) of ≈42.8 nm. Despite the benefits of bandgap tuning in mixed-cation quasi-2D perovskites, achieving phase purity remains a challenge. Our lead-free, Sn-based PeLED devices successfully exhibited phasepure EL, even in the presence of mixed phases. LED devices were fabricated by varying the 4FPEA:FA ratio, M1 and M2, and spincoating speed. The lower FA+ content in M1 promoted the formation of mixed phases (n = 1, n = 2, and $n = \infty$), whereas the higher FA^+ content in M2 resulted in the absence of the n=1 phase and predominantly n = 2 and $n = \infty$ phases, with an increased proportion of the $n = \infty$ phase. Structural and optical characterizations confirmed the mixed-phase formation, while GIWAXS studies revealed n = 1 phase enrichment at the surface and n = 2phase distributed in the bottom layers. TA spectroscopy showed no charge transfer from n = 1 to $n = \infty$ or n = 2 to $n = \infty$ in M1, whereas n = 2 to $n = \infty$ transfer was evident in **M2**. This observation suggests that charge transport in the mixed-phase quasi-2D is mediated by selective pathways. In M1, electron transport originates from the n = 1 layer and tunnels to the lower conduction band energy level of n = 2. Meanwhile, hole injection occurs from the n = 2 layer, with recombination primarily in the n = 2 phase before funnelling into the minor 3D $n = \infty$ phase. This selective recombination mechanism enables phase-pure EL, demonstrating the potential of mixed-phase quasi-2D perovskites for efficient, eco-friendly PeLED applications. In M2, dual emission was seen originating from n = 2 and $n = \infty$, alongside there was an energy funneling to the lower energy states, where the EL intensity was increased with the thickness due to the increased FASnI₃ proportions. This work emphasizes the important role that crystalline phase engineering can play in the development of PeLEDs with tuned properties.

Supporting Information

Supporting Information is available from the Wiley Online Library or from the author.

Acknowledgements

B.Z. and Q.S. would like to acknowledge MEXT KAKENHI Grant (24K01295, 26286013). B.P. acknowledges Industrieel Onderzoeksfonds



www.small-journal.com

[12] G. Vescio, J. Sanchez-Diaz, J. L. Frieiro, R. S. Sánchez, S. Hernández, A. Cirera, I. Mora-Seró, B. Garrido, ACS Energy Lett. 2022, 7, 3653.

- [13] F. Yuan, G. Folpini, T. Liu, U. Singh, A. Treglia, J. W. M. Lim, J. Klarbring, S. I. Simak, I. A. Abrikosov, T. C. Sum, A. Petrozza, F. Gao, Nat. Photonics 2024, 18, 170.
- [14] I. Chung, J.-H. Song, J. Im, J. Androulakis, C. D. Malliakas, H. Li, A. J. Freeman, J. T. Kenney, M. G. Kanatzidis, J. Am. Chem. Soc. 2012, 134, 8579
- [15] Y. Li, D. Wang, Y. Yang, C. Ding, Y. Hu, F. Liu, Y. Wei, D. Liu, H. Li, G. Shi, S. Chen, H. Li, A. Fuchimoto, K. Tosa, U. Hiroki, S. Hayase, H. Wei, Q. Shen, J. Am. Chem. Soc. 2024, 146, 3094.
- [16] X. Guan, Y. Li, Y. Meng, K. Wang, K. Lin, Y. Luo, J. Wang, Z. Duan, H. Liu, L. Yang, L. Zheng, J. Lin, Y. Weng, F. Xie, J. Lu, Z. Wei, Nat. Commun. 2024, 15, 9913.
- [17] H. Min, N. Wang, N. Chen, Y. Tong, Y. Wang, J. Wang, J. Liu, S. Wang, X. Wu, P. Yang, H. Shi, C. Zhuo, Q. Chen, J. Li, D. Zhang, X. Lu, C. Zhu, Q. Peng, L. Zhu, J. Chang, W. Huang, J. Wang, Nat. Nanotechnol. 2024, 19, 632.
- [18] G. Zhang, Y. Yang, Y. Fan, W. Tang, R. Lai, C. Zou, Y. Jin, B. Zhao, D. Di, J. Phys. Chem. Lett. 2025, 16, 2508.
- [19] J. Li, Y. Liu, J. Zeng, S. He, X. Zhu, X. Sun, Y. Jin, Adv. Mater. 2024, 37, 2414841.
- [20] V. V. Nawale, T. Sheikh, A. Nag, J. Phys. Chem. C 2020, 124, 21129.
- [21] Y. Li, H. Zhou, M. Xia, H. Shen, T. Wang, H. Gao, X. Sheng, Y. Han, Z. Chen, L. Dou, H. Zhu, E. Shi, Sci. Adv. 2023, 9, adh0517.
- [22] H. Zhu, W. Yang, Y. Reo, G. Zheng, S. Bai, A. Liu, Y.-Y. Noh, Nat. Electron. 2023, 6, 650.
- [23] Y. Chen, Y. Sun, J. Peng, J. Tang, K. Zheng, Z. Liang, Adv. Mater. 2018, 30, 1703487.
- [24] M. C. Weidman, M. Seitz, S. D. Stranks, W. A. Tisdale, ACS Nano 2016, 10, 7830.
- [25] N. Zibouche, M. S. Islam, ACS Appl. Mater. Interfaces 2020, 12, 15328.
- [26] J. Hu, L. Yan, W. You, Adv. Mater. 2018, 30, 1802041.
- [27] S. Ghosh, B. Pradhan, A. Bandyopadhyay, I. Skvortsova, Y. Zhang, C. Sternemann, M. Paulus, S. Bals, J. Hofkens, K. J. Karki, A. Materny, J. Phys. Chem. Lett. 2024, 15, 7970.
- [28] C. T. Triggs, R. D. Ross, W. Mihalyi-Koch, C. F. M. Clewett, K. M. Sanders, I. A. Guzei, S. Jin, ACS Energy Lett. 2024, 9, 1835.
- [29] J. Duan, J. Li, G. Divitini, D. Cortecchia, F. Yuan, J. You, S. Liu, A. Petrozza, Z. Wu, J. Xi, Adv. Mater. 2024, 36, 2403455.
- [30] Y. Sun, L. Zhang, N. Wang, S. Zhang, Y. Cao, Y. Miao, M. Xu, H. Zhang, H. Li, C. Yi, J. Wang, W. Huang, npj Flexible Electron. 2018,2, 12.
- [31] N. Wang, L. Cheng, R. Ge, S. Zhang, Y. Miao, W. Zou, C. Yi, Y. Sun, Y. Cao, R. Yang, Y. Wei, Q. Guo, Y. Ke, M. Yu, Y. Jin, Y. Liu, Q. Ding, D. Di, L. Yang, G. Xing, H. Tian, C. Jin, F. Gao, R. H. Friend, J. Wang, W. Huang, Nat. Photonics 2016, 10, 699.
- [32] Y. Jiang, J. Wei, M. Yuan, J. Phys. Chem. Lett. 2021, 12, 2593.
- [33] L. Zhang, C. Sun, T. He, Y. Jiang, J. Wei, Y. Huang, M. Yuan, Light: Sci. Appl. 2021, 10, 61.
- [34] Y. Yang, C. Liu, H. Kanda, Y. Ding, H. Huang, H. Chen, B. Ding, Y. Liang, X. Liu, M. Cai, P. J. Dyson, S. Dai, M. K. Nazeeruddin, Adv. Funct. Mater. 2021, 31, 2104868.
- [35] S. Parveen, K. K. Paul, P. K. Giri, ACS Appl. Mater. Interfaces 2020, 12, 6283.
- [36] F. Hao, C. C. Stoumpos, D. H. Cao, R. P. H. Chang, M. G. Kanatzidis, Nat. Photonics 2014, 8, 489.
- [37] G. C. Papavassiliou, I. B. Koutselas, A. Terzis, M. H. Whangbo, Solid State Commun. 1994, 91, 695.
- [38] C. R. Kagan, D. B. Mitzi, C. D. Dimitrakopoulos, Science 1999, 286, 945.
- [39] J. Sanchez-Diaz, R. S. Sánchez, S. Masi, M. Kreĉmarová, A. O. Alvarez, E. M. Barea, J. Rodriguez-Romero, V. S. Chirvony, J. F. Sánchez-Royo, J. P. Martinez-Pastor, I. Mora-Seró, *Joule* 2022, 6, 861.

Conflict of Interest

The authors declare no conflict of interest.

Data Availability Statement

The data that support the findings of this study are openly available in Zenodo.org at https://doi.org/10.5281/zenodo.15491738, reference number 15491738

KU Leuven (IOF)-VTI-25-00160. J.H. acknowledges funding from the

Research Foundation-Flanders (FWO Grant No. G0AHQ25N). E.M.B. ac-

knowledges the project UJI-B2022-08 EPCESBI. S.D.A. would like to thank the POLONEZ BIS project No. 2022/47/P/ST5/03261 co-funded by the

National Science Centre and the European Union's Horizon 2020 research

and innovation programme under the Marie Skłodowska-Curie grant

agreement No. 945339. This work is funded by the Ministerio de Ciencia,

Innovación y Universidades from Spanish Government through project

PLEDs, PID2022-140090OB-C21/AEI/10.13039/501100011033/FEDER,

Keywords

mixed cation perovskite, LEDs, tin perovskite, phase pure electroluminescence. Pb-free

Received: May 23, 2025 Revised: July 15, 2025 Published online: August 8, 2025

- T.-H. Han, K. Y. Jang, Y. Dong, R. H. Friend, E. H. Sargent, T.-W. Lee, Nat. Rev. Mater. 2022, 7, 757.
- [2] S. Das Adhikari, A. F. Gualdrón Reyes, S. Paul, J. Torres, B. Escuder, I. Mora-Seró, S. Masi, Chem. Sci. 2023, 14, 8984.
- [3] Y. Liu, Z. Ma, J. Zhang, Y. He, J. Dai, X. Li, Z. Shi, L. Manna, Adv. Mater. 2025. 37. 2415606.
- [4] Y. Lian, Y. Wang, Y. Yuan, Z. Ren, W. Tang, Z. Liu, S. Xing, K. Ji, B. Yuan, Y. Yang, Y. Gao, S. Zhang, K. Zhou, G. Zhang, S. D. Stranks, B. Zhao, D. Di, *Nature* 2025, 640, 62.
- [5] X.-K. Liu, W. Xu, S. Bai, Y. Jin, J. Wang, R. H. Friend, F. Gao, Nat. Mater. 2021, 20, 10.
- [6] W. Bai, T. Xuan, H. Zhao, H. Dong, X. Cheng, L. Wang, R.-J. Xie, Adv. Mater. 2023, 35, 2302283.
- [7] K. Wang, Z.-Y. Lin, Z. Zhang, L. Jin, K. Ma, A. H. Coffey, H. R. Atapattu, Y. Gao, J. Y. Park, Z. Wei, B. P. Finkenauer, C. Zhu, X. Meng, S. N. Chowdhury, Z. Chen, T. Terlier, T.-H. Do, Y. Yao, K. R. Graham, A. Boltasseva, T.-F. Guo, L. Huang, H. Gao, B. M. Savoie, L. Dou, Nat. Commun. 2023, 14, 397.
- [8] J. S. Kim, J.-M. Heo, G.-S. Park, S.-J. Woo, C. Cho, H. J. Yun, D.-H. Kim, J. Park, S.-C. Lee, S.-H. Park, E. Yoon, N. C. Greenham, T.-W. Lee, *Nature* 2022, 611, 688.
- [9] W.-F. Yang, F. Igbari, Y.-H. Lou, Z.-K. Wang, L.-S. Liao, Adv. Energy Mater. 2020, 10, 1902584.
- [10] J. Sanchez-Diaz, J. Rodriguez-Pereira, S. Das Adhikari, I. Mora-Seró, Adv. Sci. 2024, 11, 2403835.
- [11] G. Vescio, D. N. Dirin, S. González-Torres, J. Sanchez-Diaz, R. Vidal, I. P. Franco, S. D. Adhikari, V. S. Chirvony, J. P. Martínez-Pastor, F. A. Vinocour Pacheco, L. Przypis, S. Öz, S. Hernández, A. Cirera, I. Mora-Seró, M. V. Kovalenko, B. Garrido, Adv. Sustain. Syst. 2024, 8, 2400060.

SMQ

16136829, 2025, 38, Downloaded from https://onlinelibrary.wiley.com/doi/10.1002/smll.202506221 by Universitat Jaume I, Wiley Online Library on [07/11/2025]. See the Terms and Conditions, (https://onlinelibrary.wiley.com/rems-and-conditions) on Wiley Online Library for rules of use; OA articles are governed by the applicable Creative Commons License

www.advancedsciencenews.com

www.small-journal.com

- [40] Y. Li, H. Zhou, Z. Gong, M. Xia, Y. Han, X. Sheng, T. Wang, H. Zhu, E. Shi, Cell Rep. Phys. Sci. 2024, 5, 102020.
- [41] T. Du, W. Xu, S. Xu, S. R. Ratnasingham, C.-T. Lin, J. Kim, J. Briscoe, M. A. McLachlan, J. R. Durrant, J. Mater. Chem. C 2020, 8, 12648.
- [42] K. M. M. Salim, E. Hassanabadi, S. Masi, A. F. Gualdrón-Reyes, M. Franckevicius, A. Devižis, V. Gulbinas, A. Fakharuddin, I. Mora-Seró, ACS Appl. Electron. Mater. 2020, 2, 2525.
- [43] M. Rai, L. H. Wong, L. Etgar, J. Phys. Chem. Lett. 2020, 11, 8189.